Pressure Anomalies Beneath Solitary Waves with Constant Vorticity

Marcelo V. Flamarion [1,*,†], Eduardo M. Castro [2,†] and Roberto Ribeiro-Jr [2,†]

1 Unidade Acadêmica do Cabo de Santo Agostinho, UFRPE/Rural Federal University of Pernambuco, BR 101 Sul, Cabo de Santo Agostinho 54503-900, PE, Brazil
2 Departament of Mathematics, UFPR/Federal University of Paraná, Centro Politécnico, Jardim das Américas, Curitiba 81531-980, PR, Brazil
* Correspondence: marcelo.flamarion@ufrpe.br
† These authors contributed equally to this work.

Abstract: While some studies have investigated the particle trajectories and stagnation points beneath solitary waves with constant vorticity, little is known about the pressure beneath such waves. To address this gap, we investigate numerically the pressure beneath solitary waves in flows with constant vorticity. Through a conformal mapping that flats the physical domain, we develop a numerical approach that allows us to compute the pressure and the velocity field in the fluid domain. Our experiments indicate that there exists a threshold vorticity such that pressure anomalies and stagnation points occur when the intensity of the vorticity is greater than this threshold. Above this threshold, the pressure on the bottom boundary has two points of local maxima and there are three stagnation points in the flow, and below it the pressure has one local maximum and there is no stagnation point.

Keywords: constant vorticity; solitary water waves; Euler equations; pressure anomalies; stagnation points

1. Introduction

The study of water waves and their interactions with underline currents is a topic of research that has piqued the curiosity of engineers, mathematicians, physicists and oceanographers over the centuries. Although many advances have already been achieved, there are a number of basic questions that are still open.

Currents are caused mainly by density differences in the water, tidal forces and by wind [1]. Mathematically, wave–current interaction has been widely investigated under the assumption that the current is linearly sheared, i.e., it flows with constant vorticity. Physically, this can be representative of a realistic flow when waves are long compared with the depth or when waves are short compared with the length scale of the vorticity distribution [2].

Flows with constant vorticity are mainly characterized by the existence of overhanging waves, the appearance of stagnation points and the emergence of pressure anomalies.

Overhanging waves are free surface waves that are not a graph of a function. Among the numerical studies in this direction, the works of Vanden-Broeck [3,4] stand out, in which the author finds periodic and solitary overhanging waves, and more recently, the works of Dyachenko and Hur [5,6]. The existence of overhanging waves is proved rigorously by Constantin et al. [7] for periodic waves with constant vorticity, and more recently by Hur and Wheeler [8] for large or infinite depths. Although some theoretical works have already allowed overhanging solitary wave profiles in their approach [9], the rigorous proof of such wave types is still an open problem.

Stagnation points can be understood as fluid particles that are stationary in the wave moving frame. For irrotational flows, they occur at a sharp crest [10], and in flows with

constant vorticity they can emerge within the bulk of the fluid, forming a recirculation zone whose profile resembles Kelvin's cat's eye flow. The literature on stagnation points is extensive, starting with the work of Teles da Silva and Peregrine [2], the reader is referred to Ribeiro-Jr et al. for a detailed study on the appearance of stagnation points beneath periodic waves with constant vorticity. An overview of the works on stagnation point is given by Flamarion and Ribeiro-Jr [11]. More recently, Ige and Kalisch [12] investigated the particle trajectories associated with the propagation of periodic waves with constant vorticity in the framework of a new Benjamin–Bona–Mahony equation.

In irrotational flows, the pressure exerted in the bulk of the fluid beneath a Stokes wave (a periodic travelling wave with a monotone profile from the crest to the trough) attains its maximum on the bottom of the channel and below the crest. Moreover, the pressure strictly increases with the depth and strictly decreases horizontally away from a crest to a trough [13]. Notable exceptions to these features arise in rotational flows with constant vorticity: (i) the maxima and minima of the pressure may occur within the bulk of the fluid and (ii) the pressure on the bottom can be out of phase with the surface elevation [2,14–17]. The characteristics (i) and (ii) of the pressure are defined as pressure anomalies.

Although many advances have been accomplished in understanding the flow structure beneath waves with constant vorticity, it is unknown whether the pressure anomalies known for periodic waves with constant vorticity also occur for solitary waves. Strauss and Wheeler [16] proved that overhanging periodic or solitary waves must have a pressure sink, i.e., the pressure achieves its minimum within the bulk of the fluid and not on the free surface. However, this is still an open question for free surface waves that are graph of a function. This issue was raised recently by Kozlov et al. [18]. In their words, the following question was raised: "Is the pressure beneath a solitary wave in a flow with constant vorticity different from the one in the irrotational case?"

In this work, we address the question above. The novelty is twofold: (i) we find numerically that, when the vorticity crosses a threshold, the pressure on the bottom boundary caused by a solitary wave on the free surface can have two points of local maxima; (ii) we analyse in detail the appearance of stagnation points beneath solitary waves. Thus, the paper at hand responds to the question raised by Kozlov et al. [18]. Moreover, it complements the studies carried out by Vasan and Oliveras [17] and Ribeiro-Jr et al. [15], who have showed numerically the occurrence of pressure anomalies beneath periodic waves with constant vorticity and analysed the appearance of stagnation points beneath such waves. The approach used to compute the pressure and the stagnation points consists of determining a conformal mapping under which the physical domain is the image of a strip (canonical domain), then all calculations are performed through pseudo-spectral methods.

In summary, the results presented in this work are of interest to theorists and experimentalists. For a theorist, it can provide physical insights on a rigorous proof of the pressure anomalies. Likewise, it may inspire more experimental studies on this topic, since the phenomenon can be observed by manipulating the intensity of the underlying current.

For reference, this article is organized as follows: The governing equations of water waves in flows with constant vorticity are presented in Section 2. In Section 3, we describe the conformal mapping and the numerical method. Then, we present the results in Section 4 and proceed to our final considerations.

2. Governing Equations

We consider an incompressible flow of an inviscid fluid with constant density (ρ) in a two-dimensional channel with finite depth (d) under the force of gravity (g). Moreover, we assume that the flow is in the presence of a linearly sheared current (constant vorticity). Denoting the velocity field in the bulk of the fluid by $\overrightarrow{U}(x,y,t) = (u(x,y,t), v(x,y,t))$, and the free surface by $\zeta(x,t)$, this free boundary problem can be described by the Euler equations

$$\vec{U}_t + (\vec{U} \cdot \nabla)\vec{U} = -\frac{\nabla p}{\rho} - g\vec{j} \quad \text{in } -d < y < \zeta(x,t), \tag{1}$$

$$\nabla \cdot \vec{U} = 0 \quad \text{in } -d < y < \zeta(x,t), \tag{2}$$

$$p = P_{atm} \quad \text{at } y = \zeta(x,t), \tag{3}$$

$$v = \zeta_t + u\zeta_x \quad \text{at } y = \zeta(x,t), \tag{4}$$

$$v = 0 \quad \text{at } y = -d, \tag{5}$$

where $\vec{j}$ is the unitary vector $(0,1)$ and P_{atm} is the atmospheric pressure.

The assumption of constant vorticity enables us to write the velocity field as

$$\vec{U} = \vec{U_0} + \nabla\overline{\phi}, \tag{6}$$

where

$$\vec{U_0} = (ay + f, 0), \quad f \in \mathbb{R},$$

is a linear shear flow solution of (1)–(5) characterized by the flat surface $\zeta \equiv 0$ and constant vorticity $-a$. Here, $\overline{\phi}$ is the velocity potential of an irrotational perturbation of the shear flow.

Equations (1)–(5) are written in terms of $\overline{\phi}$, then non-dimensionalised via transformation (7)

$$\begin{aligned}
x &= dx', & \zeta &= d\zeta', & \Omega &= \frac{ad}{\sqrt{dg}}, \\
y &= dy', & \overline{\phi} &= d\sqrt{dg}\phi', & p &= P_0 + \rho g d p', \\
t &= \sqrt{\frac{d}{g}}t', & \overline{\psi} &= d\sqrt{dg}\psi', & F &= \frac{f}{\sqrt{dg}}.
\end{aligned} \tag{7}$$

Dropping the prime notation, this gives us the dimensionless version of the governing equations

$$\Delta\overline{\phi} = 0 \text{ in } -1 < y < \zeta(x,t), \tag{8}$$

$$\zeta_t + (\Omega\zeta + F + \overline{\phi}_x)\zeta_x = \overline{\phi}_y \text{ at } y = \zeta(x,t), \tag{9}$$

$$\overline{\phi}_t + \frac{1}{2}(\overline{\phi}_x^2 + \overline{\phi}_y^2) + (\Omega\zeta + F)\overline{\phi}_x + \zeta - \Omega\overline{\psi} = B(t) \text{ at } y = \zeta(x,t), \tag{10}$$

$$\overline{\phi}_y = 0 \text{ at } y = -1, \tag{11}$$

where $-\Omega$ is the dimensionless vorticity, F is the Froude number and the pressure in the fluid body is given by

$$p = -\left(\overline{\phi}_t + \frac{1}{2}(\overline{\phi}_x^2 + \overline{\phi}_y^2) + (\Omega\zeta + F)\overline{\phi}_x + \zeta - a\overline{\psi} - B(t)\right). \tag{12}$$

For the study of traveling wave solutions, it is convenient to eliminate time from the problem by passing to a moving frame

$$X = x - ct \quad \text{and} \quad Y = y,$$

where c is the wave speed, to be determined a posteriori. In this new moving reference frame, the wave is stationary and the flow is steady. Taking this new frame of reference into account, Equations (8)–(12) are written as

$$\Delta\overline{\phi} = 0 \quad \text{in } -1 < Y < \zeta(X), \tag{13}$$

$$-c\zeta_X + (F + \Omega\zeta + \overline{\phi}_X)\zeta_X = \overline{\phi}_Y \quad \text{at } Y = \zeta(X), \tag{14}$$

$$-c\overline{\phi}_X + \frac{1}{2}(\overline{\phi}_X^2 + \overline{\phi}_Y^2) + (\Omega\zeta + F)\overline{\phi}_X + \zeta - \Omega\overline{\psi} = B \quad \text{at } Y = \zeta(X), \tag{15}$$

$$\overline{\phi}_Y = 0 \quad \text{at } Y = -1, \tag{16}$$

and

$$p = -\left(-c\overline{\phi}_X + \frac{1}{2}(\overline{\phi}_x^2 + \overline{\phi}_y^2) + (\Omega\zeta + F)\overline{\phi}_x + \zeta - \Omega\overline{\psi} - B\right). \tag{17}$$

We assume that $\zeta(X)$ is a solitary wave whose crest is located at $X = 0$ and satisfies

$$\zeta(X) \to 0 \quad \text{as} \quad |X| \to \infty. \tag{18}$$

In the following, we present a numerical scheme to compute the solutions of the system (13)–(16) and to calculate the pressure in the fluid body via Formula (17).

3. Conformal Mapping and the Numerical Method

Since $\zeta(X)$ decays to zero as $|X| \to \infty$, we can truncate its infinite domain to a finite one $[-\lambda/2, \lambda/2]$ with $\lambda > 0$, and approximate the boundary conditions by periodic conditions. Then, we can solve Equations (13)–(16) through the conformal mapping technique introduced by Dyachenko et al. [19], which has been widely applied in free boundary problems [15,20,21]. This strategy consists of using conformal mapping from a strip of length L and width D (canonical domain) onto the flow domain of the solitary wave $\{(X,Y) \in \mathbb{R}^2, -\lambda/2 \le X \le \lambda/2 \text{ and } -1 \le Y \le \zeta(X)\}$. This map is such that in the canonical domain, the free boundary problem (13)–(16) can be solved numerically by the use of a spectral collocation method and Newton's method.

3.1. Conformal Mapping

Consider the conformal mapping

$$Z(\xi, \eta) = X(\xi, \eta) + iY(\xi, \eta), \tag{19}$$

under which the strip $\{(\xi, \eta) \in \mathbb{R}^2; -L/2 \le \xi \le L/2 \text{ and } -D \le \eta \le 0\}$ is mapped onto the flow domain, as in Figure 1. The constant D will be determined so that the canonical and the physical domain have the same length. Since Z is taken to be conformal, thus analytical, X and Y are actually conjugate harmonic functions, whereas the mapping's Jacobian is given by

$$J = X_\xi^2 + Y_\xi^2. \tag{20}$$
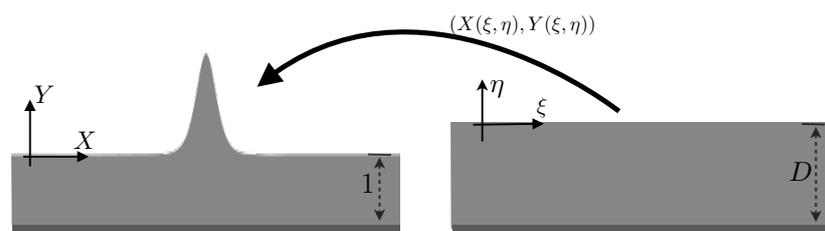
Figure 1. Illustrative depiction of the conformal mapping. The free surface is flattened out in the canonical domain.

A central characteristic of this mapping is given by the way that the boundary curves from each domain are related

$$\begin{cases} Y(\xi, 0) = \zeta(X(\xi, 0)), \\ Y(\xi, -D) = -1, \end{cases} \tag{21}$$

which serves as Dirichlet data for the Laplace equation for $Y(\xi, \eta)$. By denoting $\mathbf{Y}(\xi) = Y(\xi, 0)$ and $\mathbf{X}(\xi) = X(\xi, 0)$, the traces of the respective harmonic functions along $\eta = 0$, we have

$$Y(\xi, \eta) = \mathcal{F}^{-1}\left[\frac{\sinh(k(\eta + D))}{\sinh(kD)} \mathcal{F}(\mathbf{Y}) \right] + \frac{(\eta + D)\langle \mathbf{Y} \rangle + \eta}{D}, \quad k \neq 0, \tag{22}$$

where $k = k(j) = (\pi/L)j$, for $j \in \mathbb{Z}$, $\mathcal{F}$ is the Fourier transform in ξ-variable given by

$$\mathcal{F}(f(\xi)) = \hat{f}(k) = \frac{1}{L} \int_{-L/2}^{L/2} f(\xi) e^{-ik\xi} d\xi,$$

$$\mathcal{F}^{-1}(\hat{f}(k)) = f(\xi) = \sum_{j \in \mathbb{Z}} \hat{f}(k) e^{ik\xi},$$

and $\langle \cdot \rangle$ denotes the average defined by

$$\langle \mathbf{Y} \rangle = \frac{1}{L} \int_{-L/2}^{L/2} \mathbf{Y}(\xi) d\xi.$$

By differentiating Equation (22) with respect to η and integrating the Cauchy–Riemann equation $X_\xi = Y_\eta$, we obtain

$$X(\xi, \eta) = \left(\frac{1 + \langle \mathbf{Y} \rangle}{D} \right) \xi - \mathcal{F}^{-1}\left[\frac{i \cosh(k(\eta + D))}{\sinh(kD)} \mathcal{F}(\mathbf{Y}) \right], \quad k \neq 0. \tag{23}$$

The canonical depth D can be fixed if we require that both canonical and physical domains have the same length. Let L and λ be the respective lengths, thus

$$\mathbf{X}(\xi = L/2) - \mathbf{X}(\xi = -L/2) = \lambda.$$

It follows from (23) that this restriction leads to the relation

$$D = 1 + \langle \mathbf{Y} \rangle. \tag{24}$$

A reader interested in further details on the conformal mapping presented here should consult Flamarion and Ribeiro-Jr [22] for conformal mapping in the context of uneven topographies and its accuracy.

By denoting $\phi(\xi, \eta) = \overline{\phi}(X(\xi, \eta), Y(\xi, \eta))$ and $\psi(\xi, \eta) = \overline{\psi}(X(\xi, \eta), Y(\xi, \eta))$, the governing Equations (13)–(16) can be written in the canonical coordinate system. Subsequently, by combining Equations (14) and (15), a single equation for the free surface wave can be obtained, namely,

$$\begin{aligned} -\frac{c^2}{2} + \frac{c^2}{2J} + \mathbf{Y} + \frac{(\mathcal{C}[(\Omega\mathbf{Y} + F)\mathbf{Y}_\xi])^2}{2J} - \frac{\mathcal{C}[(\Omega\mathbf{Y} + F)\mathbf{Y}_\xi]}{J}(c - (\Omega\mathbf{Y} + F)\mathbf{X}_\xi) \\ -\frac{(\Omega\mathbf{Y} + F)^2 \mathbf{Y}_\xi^2}{2J} - \frac{c(\Omega\mathbf{Y} + F)\mathbf{X}_\xi}{J} + Fc + \Omega\left(\frac{\Omega\mathbf{Y}}{2} + F \right)\mathbf{Y} + \Omega M = B, \end{aligned} \tag{25}$$

where $\mathcal{C}$ is the periodic Hilbert transform on a strip whose Fourier symbol is $i\coth(kD)$ and

$$M = \left\langle c\mathbf{Y} - \left(\frac{\Omega\mathbf{Y}^2}{2} + F\mathbf{Y} \right) \right\rangle.$$

Details of the derivation of this equation are given in the Appendix B.

Observe that $\mathbf{X}_\xi = 1 - \mathcal{C}_0[\mathbf{Y}_\xi]$ and $J = \mathbf{X}_\xi^2 + \mathbf{Y}_\xi^2$ are given in terms of $\mathbf{Y}(\xi)$. Consequently, Equation (25) has as unknowns $\mathbf{Y}(\xi)$, c, D and B. It is the aim of the next section to describe a numerical approach for computing solitary waves.

3.2. Numerical Method

Up to this point, we have transformed the free boundary problem (13)–(16) into a nonlinear system of two equations ((24) and (25)) and four unknowns $\mathbf{Y}(\xi)$, c, D and B. In order to obtain a system that can be handled by Newton's method, we add two extra equations.

We fix the amplitude A of the wave through

$$Y(0) - Y(-L/2) = A, \tag{26}$$

and based on the limit (18), we impose that

$$Y(-L/2) = 0. \tag{27}$$

Consider a discrete version of Equations (24)–(27) as follows. Let us take an evenly spaced grid in the ξ-axis in the canonical domain, say

$$\xi_j = -L/2 + (j-1)\Delta\xi, \quad j = 1, ..., N, \quad \text{where } \Delta\xi = L/N, \tag{28}$$

with N being even. We impose symmetry about $\xi = 0$ so that $Y_j = Y_{N-j+2}$, where $Y_j = \mathbf{Y}(\xi_j)$. Fixing Ω and F, we have $N/2 + 4$ unknowns: $Y_1, \cdots, Y_{N/2+1}$, c, D and B. We satisfy Equation (25) at the grid points (28). The Fourier modes are computed by the Fast Fourier Transform (FFT) and derivatives in the ξ-variable are performed spectrally [23]. This yields a system with $N/2 + 1$ equations

$$\mathcal{G}_j(Y_1, \cdots, Y_{N/2+1}, c, D, B) = 0 \quad j = 1, \cdots, N/2 + 1.$$

Equation (24) is discretized using the trapezoidal rule, which leads to the equation

$$\mathcal{G}_{N/2+2}(Y_1, \cdots, Y_{N/2+1}, c, D, B) = \frac{Y_1 + Y_{N/2+1}}{2} + \sum_{j=2}^{N/2} Y_j + 1 - D = 0.$$

Finally, we satisfy Equations (26) and (27), resulting in a system of $N/2 + 4$ equations and $N/2 + 4$ unknowns,

$$\mathcal{G}_{N/2+3}(Y_1, \cdots, Y_{N/2+1}, c, D, B) = Y_{N/2+1} - Y_1 - A = 0,$$

$$\mathcal{G}_{N/2+4}(Y_1, \cdots, Y_{N/2+1}, c, D, B) = Y_1 = 0.$$

The system is solved by Newton's method, where our initial guess is taken to be the well-known solitary wave solution for the classical (irrotational) Korteweg–de Vries equation, that is

$$\mathbf{Y}(\xi) = A_0 \operatorname{sech}^2\left(\sqrt{3A_0/4}\,\xi\right), \quad c = 1 + \frac{A_0}{2},$$

where A_0 is chosen to be small. From there, the idea is to make use of the continuation technique in A and Ω, where the prior converged solution is fed as an initial guess to a

new solution. The Jacobian matrix of the system is computed by finite difference and the stopping criterion for the Newton's method is

$$\frac{\sum_{j=1}^{N/2+4} |\mathcal{G}_j|}{N/2 + 4} < 10^{-10}.$$

In all experiments performed we used $L = 1500$, which is important to make sure that the method indeed converges to a solitary wave solution.

4. Results

In Section 4.1, we present some solitary waves computed through our numerical method. A comparison between such waves with a weakly nonlinear KdV equation is performed in order to provide a validation of our numerical procedure. Then, the main results of the paper are discussed in Section 4.2.

4.1. Steady Waves

Several numerical computations are available and provide a detailed characterization of the shape of the free surface wave in flows with constant vorticity. More specifically, it is known that the crests of the waves become rounder as Ω decreases. This has been shown for periodic travelling waves [2,3,6,15,24] and for solitary waves [4].

Figure 2 displays various wave profiles for different vorticity values. As can be seen, the numerical method captures the well-known characteristics of waves with vorticity: more rounded or cuspidate profiles depending on the Ω sign. Although the computational domain used was $L = 1500$, for visualization purposes the plot window was chosen to be 50 units long. Moreover, for each choice of Ω, the Froude number was fixed as $F = \Omega/2$. This implies cancelling the average mass flow of the stream $\vec{U}_0 = (\Omega Y + F, 0)$. The choice of F has no impact on the shape of wave nor on the location of the stagnation points and the appearance of pressure anomalies.
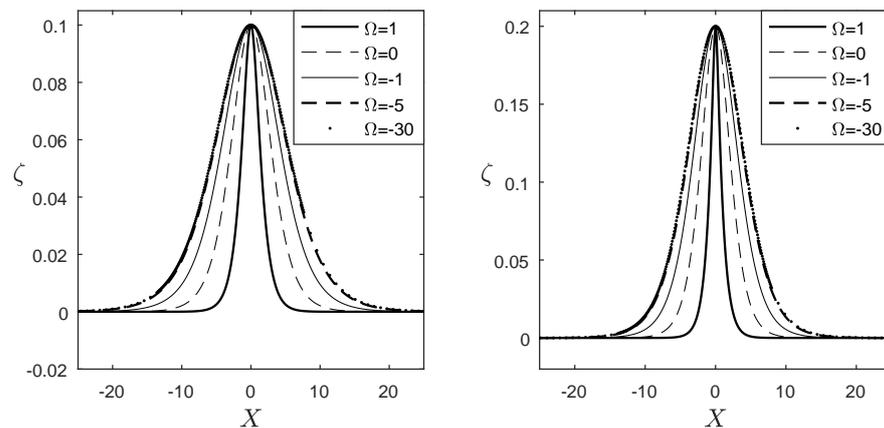
Figure 2. Wave profiles with amplitudes $A = 0.1$ (**left**) and $A = 0.2$ (**right**).

Furthermore, vorticity also has a straightforward and expected effect on the velocity of the waves: greater vorticity implies greater velocity across the amplitude spectrum, a trend that matches with the well-known dispersion relation for linear long waves, as depicted in Figure 3. From that same figure, it is also notable that even though the method captures waves with negative Ω, which are considerably large in modulus, convergence stops earlier in the positive direction. This phenomenon is in a large part explained by the loss of solution

regularity in a neighbourhood of $X = 0$ when Ω becomes more positive, something hinted at by Figure 2. The closed formula for the velocity shown in dashed lines in Figure 3 is given by

$$c_{lin} = F - \frac{\Omega}{2} + \sqrt{\frac{\Omega^2}{4} + 1}.$$
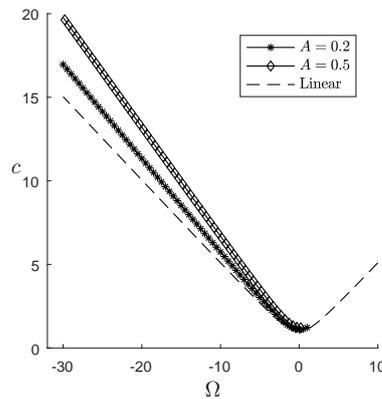
Figure 3. The wave speed as function of Ω for different values of A.

Beyond the linear theory, another model that can be used for comparison purposes is the weakly nonlinear KdV equation. In what follows, we are interested in investigating how the velocities are influenced by the increase in amplitude for a fixed vorticity. For small amplitudes, it is expected that the waves computed should be similar to the sech^2-type solution of the KdV equation.

Regarding the analysis of the KdV model in the presence of vorticity, we refer to the work of Guan [25]. The formulation presented by this author is used as a benchmark for our numerical solutions.

For a given choice of parameters Ω and A, Figure 4 indicates the distance between our solutions and the analytical solution determined by the KdV equation. The dashed line displays the wave speed from the KdV solution after scaling to the Euler regime. As expected, we see a very close wave speed whenever A is small, but the overall pattern of speed/amplitude relation in the case of the Euler solutions present a clear deviation from the linear distribution found in KdV. In particular, around $A = 0.15$ and $A = 0.2$ we see a slight takeoff from the Euler regime in comparison to the KdV, while it is interesting to observe that the general aspect of this "takeoff curve" remains unchanged when we vary Ω. For the interested reader, a study of the resolution of the numerical method is presented in Appendix A.
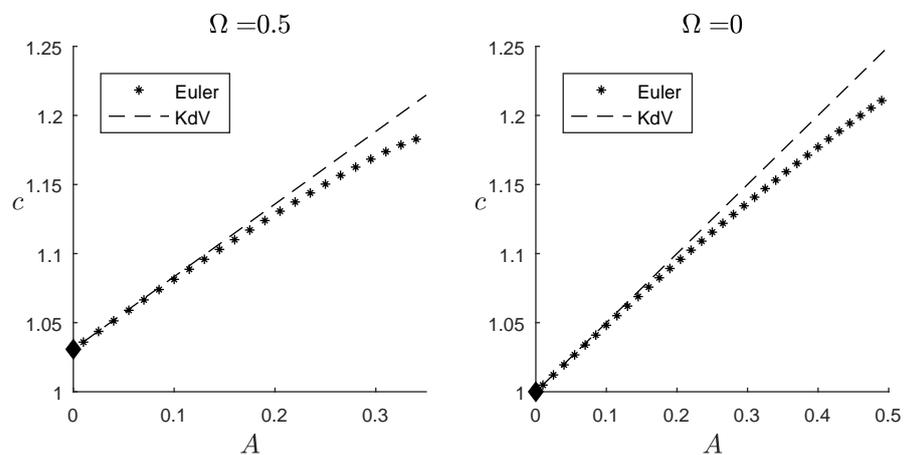
Figure 4. *Cont.*
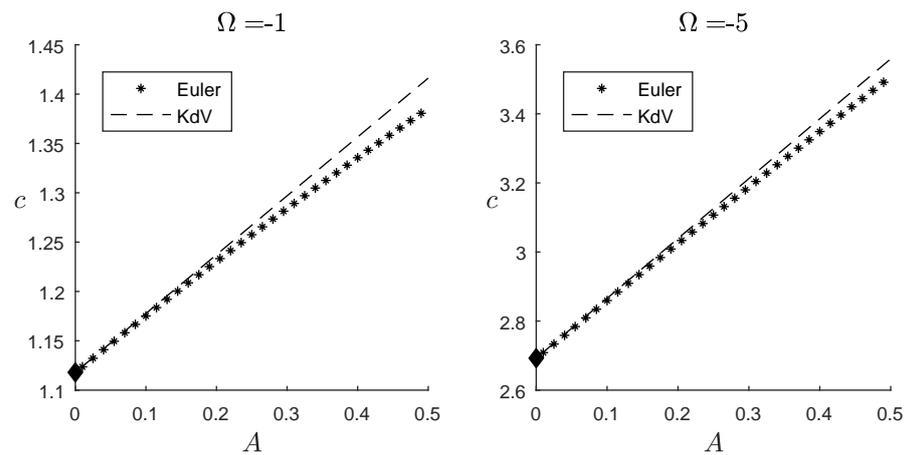
Figure 4. The wave speed as function of the wave amplitude for different choices of vorticity. Diamond denotes the linear speed c_{lin}.

4.2. Pressure in the Bulk of the Fluid

It is well known in the literature that pressure anomalies beneath nonlinear periodic waves are connected to the emergence of stagnation points [2,15,17]. Starting from this point, we first investigated the appearance of stagnation points in terms of the intensity of the vorticity parameter (Ω), then analysed the pressure within the bulk of the fluid. For this purpose, we fixed solitary waves with amplitude $A = 0.2$, $F = \Omega$ and let the vorticity vary. This choice of F leads to a background flow $(\Omega Y + F, 0)$ with zero velocity at the bottom.

Our first numerical essay consists of computing the phase portrait for different values of the vorticity parameter—this is depicted in Figure 5. The markers represent the position of the stagnation points. We find that the stagnation points first appear on the bottom and below the crest for a critical value $\Omega^\star \approx -2.4967$. For $\Omega > \Omega^\star$, there are no stagnation points in the bulk of the fluid. Nonetheless, for $\Omega < \Omega^\star$, we obtain a flow with three stagnation points: two saddles located at the bottom and one centre located within the bulk of the fluid and below the crest, forming a region with closed streamlines which is described as a single Kelvin cat's eye structure. As the vorticity becomes stronger, this structure becomes wider, i.e, the saddles remain on the bottom moving away from each other and the centre moves upwards.
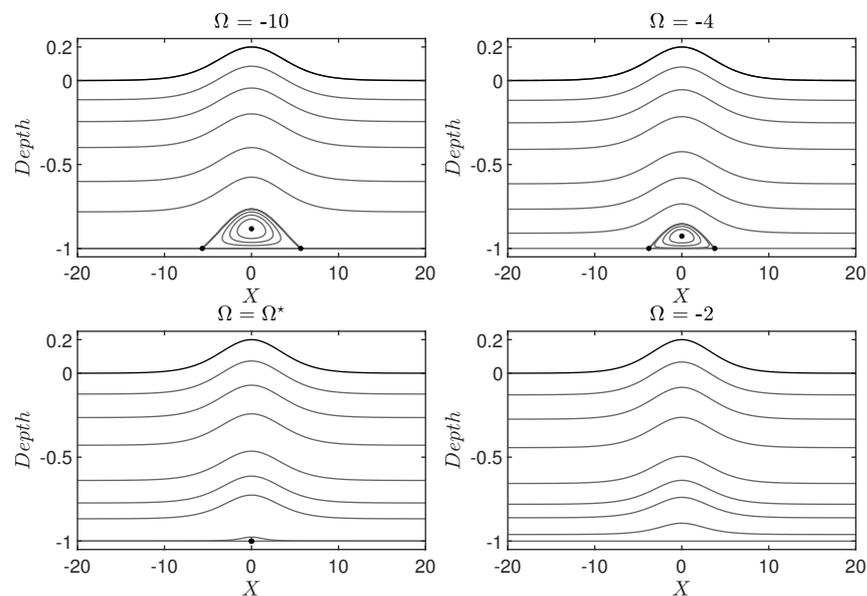
Figure 5. Phase portraits for different values of the vorticity parameter. Circles correspond to the location of the stagnation points. $\Omega^\star \approx -2.4967$.

Figure 6 shows the pressure contours and the pressure on the bottom boundary for the same waves depicted in Figure 5. We notice that, according to the value of Ω, the following anomalies occur: (i) the maximum pressure value may not be attained at the bottom and below the crest; (ii) the minimum pressure value may be attained within the bulk of the fluid; and (iii) the pressure on the bottom boundary may have two local maxima. These anomalies have been observed for nonlinear periodic waves [2,15,17] and for overhanging solitary waves [16], but to the best of our knowledge this the first time that such results have been reported for solitary waves that are graph of a function. These results indicate that the anomalies in the pressure and the stagnation points are somehow related. Moreover, pressure anomalies and stagnation points occur when a threshold vorticity is achieved. However, a detailed theoretical study is necessary to explain such a phenomenon.
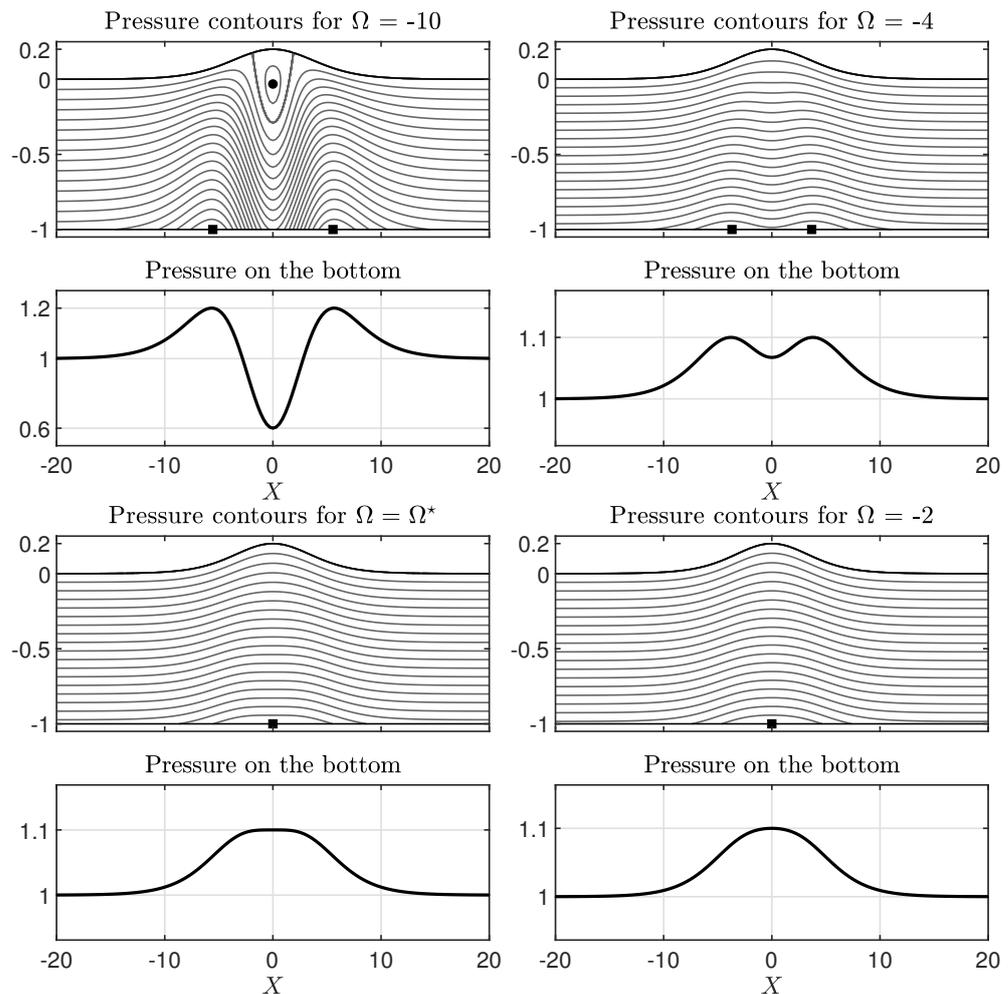
Figure 6. Pressure beneath the solitary wave with amplitude $A = 0.2$ and its corresponding pressure on the bottom boundary. Circle and square markers indicate the location of global minima and maxima of the pressure, respectively.

5. Conclusions

In the present work, we have studied the pressure beneath solitary waves in flows with constant vorticity. Our results indicate that there exists a threshold vorticity such that pressure anomalies and stagnation points occur when the intensity of the vorticity is greater than the threshold. More specifically, when the vorticity is below this threshold, the pressure on the bottom boundary has one local maximum and there is no stagnation point in the flow. Once the vorticity crosses this threshold, the pressure on the bottom boundary has two local maxima and the flow has three stagnation points (one centre and two saddles).

Author Contributions: Conceptualization, M.V.F., E.M.C. and R.R.-J.; Methodology, M.V.F., E.M.C. and R.R.-J.; Writing—original draft, M.V.F., E.M.C. and R.R.-J.; Writing—review & editing, M.V.F., E.M.C. and R.R.-J. All authors have read and agreed to the published version of the manuscript.

Funding: The author E.M.C. is grateful for the financial support provided by CAPES Foundation (Coordination for the Improvement of Higher Education Personnel) during part of the development of this work.

Institutional Review Board Statement: Not applicable.

Informed Consent Statement: Informed consent was obtained from all subjects involved in the study.

Data Availability Statement: Not applicable.

Acknowledgments: M.V.F. and R.R.J. are grateful to IMPA for hosting them as visitors during the 2023 Post-Doctoral Summer Program.

Conflicts of Interest: The authors declare no conflict of interest.

Abbreviations

In this section, we provide a list of the main symbols that have been utilized throughout the text.

Symbol	Meaning
B	Bernoulli constant
c	Wave speed
$\mathcal{C}[\cdot]$	The periodic Hilbert transform on a strip of width D
D	Width of strip that corresponds to the canonical domain
F	Froude number
L	Length of the canonical domain
p	pressure in fluid body
(ξ, η)	Coordinate system in the canonical domain
$(X(\xi, \eta), Y(\xi, \eta))$	Conformal mapping that applies a strip of width D in the physical domain.
$(\mathbf{X}(\xi), \mathbf{Y}(\xi)) = (X(\xi, 0), Y(\xi, 0))$	Free surface wave profile written in terms of the conformal mapping
$-\Omega$	Dimensionless vorticity
(x, y)	Laboratory frame of reference
$\zeta(X)$	Free surface wave profile in the moving frame $X = x - ct$ and $Y = y$
$\overline{\phi}$	Velocity potential for the irrotational part of the velocity field
$\overline{\psi}$	Harmonic conjugate function of $\overline{\phi}$
$\phi(\xi, \eta) = \overline{\phi}(X(\xi, \eta), Y(\xi, \eta))$	Potential $\overline{\phi}$ written in the coordinate system (ξ, η)
$\psi(\xi, \eta) = \overline{\psi}(X(\xi, \eta), Y(\xi, \eta))$	Function $\overline{\psi}$ written in the coordinate system (ξ, η)
$\mathbf{\Phi}(\xi) = \psi(\xi, 0)$	Potential ϕ evaluated at $\eta = 0$
$\mathbf{\Psi}(\xi) = \psi(\xi, 0)$	Function ψ evaluated at $\eta = 0$

Appendix A. Resolution Study

In what follows, we show that the method is independent of the grid size by calculating the distance between outputs for different choices of $\Delta\xi$. These experiments were performed for waves with amplitude $A = 0.2$. We take the reference grid as $\Delta\xi^* = 0.0458$, the finest resolution computed.

In Table A1, we denote by $\zeta_{\Delta\xi}$ the wave profile and by $c_{\Delta\xi}$ the wave speed obtained from Newton's method using a grid with size $\Delta\xi$. In addition, we consider ζ^* and c^* as the wave profile and its speed computed in the finest grid. These experiments were performed for waves with amplitude $A = 0.2$. Note that for $\Omega = 1$, the numerical scheme requires more resolution to approximate the solution with more accuracy. This can be explained by a combination of two factors: (i) the emergence of cusps and (ii) the issue of crowding phenomenon present in conformal mappings. For this reason, finer grids are necessary to accurately compute waves in the presence of currents where Ω is positive.

Table A1. Resolution study for waves of amplitude $A = 0.2$.

Ω	$\Delta\xi$	$\dfrac{\|\zeta_{\Delta\xi} - \zeta^*\|_2}{\|\zeta^*\|_2}$	$\dfrac{|c_{\Delta\xi} - c^*|}{|c^*|}$
0	0.0916	1.6×10^{-10}	2.5×10^{-12}
	0.1831	4.6×10^{-10}	7.4×10^{-12}
	0.3662	6.7×10^{-8}	5.6×10^{-10}
	0.7324	1.2×10^{-4}	5.2×10^{-6}
−1	0.0916	5.4×10^{-13}	2.1×10^{-14}
	0.1831	5.7×10^{-13}	1.0×10^{-14}
	0.3662	1.5×10^{-12}	1.3×10^{-14}
	0.7324	1.2×10^{-7}	1.8×10^{-9}
1	0.0916	6.8×10^{-5}	1.0×10^{-6}
	0.1831	0.0027	1.7×10^{-4}
	0.3662	0.0477	0.0015
	0.7324	0.1164	0.0102

Finally, to provide an indication of the accuracy of our numerical method, we conducted a comparison between our numerical results and those obtained by Teles da Silva and Peregrine [2] for the relationship between the wave speed and wave amplitude. Specifically, we set the Froude number F = 0 and compared the graphs of the wave speed as a function of wave amplitude for flows with $\Omega = -1, 0, 0.5$ with Figures 9 and 10 presented in Teles da Silva and Peregrine's work. The comparison is illustrated in Figure A1, which demonstrates a strong agreement between the two methods.
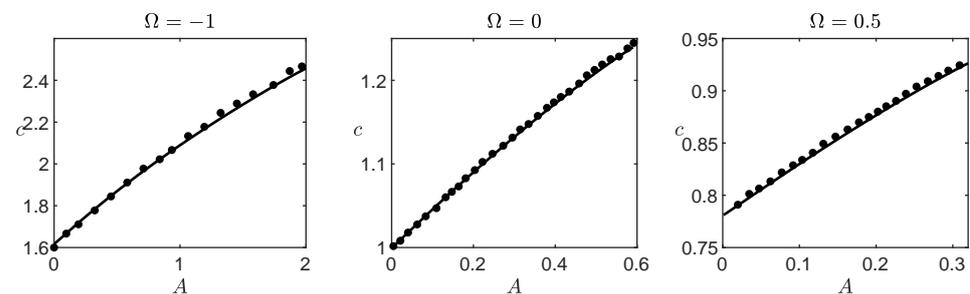
Figure A1. Comparison between our numerical results and those obtained by Teles da Silva and Peregrine [2] for the wave speed as a function of wave amplitude. The solid line represents the results from our numerical method, while the dots correspond to the results computed by Teles da Silva and Peregrine.

Appendix B. The Free Surface Wave in the Canonical Coordinate System

In this section, we give more details on the derivation of Equation (25). We start by noticing that the Laplace equation is conformally invariant. So, denoting by $\phi(\xi, \eta) = \overline{\phi}(X(\xi, \eta), Y(\xi, \eta))$ and $\psi(\xi, \eta) = \overline{\psi}(X(\xi, \eta), Y(\xi, \eta))$ the potential and its harmonic conjugate in the canonical coordinates, one can easily obtain the following:

$$
\begin{aligned}
\phi_{\xi\xi} + \phi_{\eta\eta} &= 0 \qquad && \text{in } -D < \eta < 0, \\
\phi &= \mathbf{\Phi}(\xi) \qquad && \text{at } \eta = 0, \\
\phi_\eta &= 0 \qquad && \text{at } \eta = -D,
\end{aligned}
$$

and

$$
\begin{aligned}
\psi_{\xi\xi} + \psi_{\eta\eta} &= 0 \qquad && \text{in } -D < \eta < 0, \\
\psi &= \mathbf{\Psi}(\xi) \qquad && \text{at } \eta = 0, \\
\psi &= Q \qquad && \text{at } \eta = -D,
\end{aligned}
$$

where Q is an arbitrary constant. The formulas for $\phi(\xi, \eta)$ and $\psi(\xi, \eta)$ can be found in a similar fashion to that worked out for $X(\xi, \eta)$ and $Y(\xi, \eta)$, which yields

$$\phi(\xi, \eta) = \mathcal{F}^{-1}\left[\frac{\cosh(k(\eta + D))}{\cosh(kD)}\mathcal{F}(\boldsymbol{\Phi})\right],$$

$$\psi(\xi, \eta) = \mathcal{F}^{-1}\left[\frac{\sinh(k(\eta + D))}{\sinh(kD)}\mathcal{F}(\boldsymbol{\Psi})\right] - Q\frac{\eta}{D}.$$

Using the Cauchy–Riemman equation $\phi_\xi = \psi_\eta$ and evaluating along $\eta = 0$, we find that

$$\boldsymbol{\Phi}_\xi(\xi) = \mathcal{F}^{-1}\left[-i\coth(kD)\mathcal{F}_k(\boldsymbol{\Psi}_\xi)\right]. \tag{A1}$$

For simplicity, we make use of the Fourier operator $\mathcal{C}[\cdot]$ defined as follows: given a function $h(\xi)$,

$$\mathcal{C}[h(\xi)] = \mathcal{C}_0[h(\xi)] + \lim_{k\to 0} i\coth(kD)\hat{h}(k), \tag{A2}$$

where $\mathcal{C}_0[\,\cdot\,] = \mathcal{F}^{-1}\mathcal{H}\mathcal{F}[\,\cdot\,]$, with $\mathcal{H}$ given by

$$\mathcal{H}(k) = \begin{cases} i\coth(kD), & k \neq 0 \\ 0, & k = 0. \end{cases} \tag{A3}$$

For the particular case of $\mathcal{C}[\cdot]$ evaluated at $h_\xi(\xi)$, we have

$$\mathcal{C}[f_\xi(\xi)] = \mathcal{C}_0[h_\xi(\xi)] - \frac{\hat{h}(0)}{D}, \tag{A4}$$

With this notation, we obtain from relations (23), (24) and (A1) that

$$\mathbf{X}_\xi = 1 - \mathcal{C}_0[\mathbf{Y}_\xi] \tag{A5}$$

$$\boldsymbol{\Phi}_\xi = -\mathcal{C}_0[\boldsymbol{\Psi}_\xi] + \frac{\hat{\mathbf{Y}}(0)}{D}. \tag{A6}$$

Performing straightforward calculations, we obtain that the kinematic condition (14) and Bernoulli law (15) in canonical coordinates are given by

$$\boldsymbol{\Psi}_\xi = c\mathbf{Y}_\xi - (\Omega\mathbf{Y} + F)\mathbf{Y}_\xi, \tag{A7}$$

$$-c\frac{\boldsymbol{\Phi}_\xi \mathbf{X}_\xi + \boldsymbol{\Psi}_\xi \mathbf{Y}_\xi}{J} + \frac{1}{2J}(\boldsymbol{\Phi}_\xi^2 + \boldsymbol{\Psi}_\xi^2) + \mathbf{Y} + (\Omega\mathbf{Y} + F)\frac{\boldsymbol{\Phi}_\xi \mathbf{X}_\xi + \boldsymbol{\Psi}_\xi \mathbf{Y}_\xi}{J} - \Omega\boldsymbol{\Psi} = 0. \tag{A8}$$

Then, integrating (A7), we obtain

$$\boldsymbol{\Psi} = c\mathbf{Y} - \left(\frac{\Omega\mathbf{Y}^2}{2} + F\mathbf{Y}\right) + M, \tag{A9}$$

where M is an arbitrary constant. In order to simplify the use of the formula (A6), we choose $\boldsymbol{\Psi}$ so that $\hat{\boldsymbol{\Psi}}(0) = 0$. This leads naturally to

$$M = \left\langle c\mathbf{Y} - \left(\frac{\Omega\mathbf{Y}^2}{2} + F\mathbf{Y}\right)\right\rangle.$$

Hence,

$$\boldsymbol{\Phi}_\xi = -\mathcal{C}_0[\boldsymbol{\Psi}_\xi]. \tag{A10}$$

By substituting Equation (A9) and (A10) into (A8), then Equation (A7) into the resulting equation, we obtain a single equation for the free surface

$$-\frac{c^2}{2} + \frac{c^2}{2J} + \mathbf{Y} + \frac{(\mathcal{C}[(\Omega\mathbf{Y}+F)\mathbf{Y}_\xi])^2}{2J} - \frac{\mathcal{C}[(\Omega\mathbf{Y}+F)\mathbf{Y}_\xi]}{J}(c - (\Omega\mathbf{Y}+F)\mathbf{X}_\xi)$$
$$-\frac{(\Omega\mathbf{Y}+F)^2\mathbf{Y}_\xi^2}{2J} - \frac{c(\Omega\mathbf{Y}+F)\mathbf{X}_\xi}{J} + Fc + \Omega\left(\frac{\Omega\mathbf{Y}}{2} + F\right)\mathbf{Y} + \Omega M = B,$$

References

1. Dalrymple, R.A. *Water Wave Models and Wave Forces with Shear Currents*; Technical Report No. 20; Coastal and Oceanographic Engineering Laboratory, University of Florida: Gainesville, FL, USA, 1973.
2. Teles Da Silva, A.F.; Peregrine, D.H. Steep, steady surface waves on water of finite depth with constant vorticity. *J. Fluid Mech.* **1988**, *195*, 281–302. [CrossRef]
3. Vanden-Broeck, J.-M. Periodic waves with constant vorticity in water of infinite depth. *IMA J. Appl. Maths* **1996**, *56*, 207–217. [CrossRef]
4. Vanden-Broeck, J.-M. Steep solitary waves in water of finite depth with constant vorticity. *J. Fluid Mech.* **1994**, *274*, 339–348. [CrossRef]
5. Dyachenko, S.A.; Hur, V.M. Stokes waves with constant vorticity: Folds, gaps and fluid bubbles. *J. Fluid Mech.* **2019**, *878*, 502–521. [CrossRef]
6. Dyachenko, S.A.; Hur, V.M. Stokes waves with constant vorticity: I. Numerical computation. *Stud. Appl. Maths* **2019**, *142*, 162–189. [CrossRef]
7. Constantin, A.; Strauss, W.; Vărvărucă, E. Global bifurcation of steady gravity water waves with critical layers. *Acta Math.* **2016**, *217*, 195–262. [CrossRef]
8. Hur, V.M.; Wheeler, M. Overhanging and touching waves in constant vorticity flows. *J. Differ. Equations* **2022**, *338*, 572–590. [CrossRef]
9. Haziot, S.V.; Wheeler, M. Large-amplitude steady solitary water waves with constant vorticity. *arXiv* **2021**, arXiv:2110.04901.
10. Varvaruca, E. Singularities of Bernoulli free boundaries. Commun. Partial Differ. *Equations* **2006**, *31*, 1451–1477.
11. Flamarion, M.V.; Ribeiro, R., Jr. Solitary Waves on Flows with an Exponentially Sheared Current and Stagnation Points. *Q. J. Mech. Appl. Math.* **2023**, *76*, 79–91. [CrossRef]
12. Ige, O.E.; Kalisch, H. Particle trajectories in a weakly nonlinear long-wave model on a shear flow. *Appl. Numer. Math.* **2023**, *in press*. [CrossRef]
13. Constantin, A.; Strauss, W. Pressure beneath a Stokes wave. *Comm. Pure. Appl. Math.* **2010**, *63*, 533–557. [CrossRef]
14. Ali, A.; Kalisch, H. Reconstruction of the pressure in long-wave models with constant vorticity. *Eur. J. Mech. B Fluids* **2013**, *37*, 187–194. [CrossRef]
15. Ribeiro, R., Jr.; Milewski, P.A.; Nachbin, A. Flow structure beneath rotational water waves with stagnation points. *J. Fluid. Mech.* **2017**, *812*, 792–814. [CrossRef]
16. Strauss, W.A.; Wheeler, M. Bound on the slope of steady water waves with favorable vorticity. *Arch. Rat. Mech. Anal.* **2016**, *222*, 1555–1580. [CrossRef]
17. Vasan, V.; Oliveras, K. Pressure beneath a travelling wave with constant vorticity. *DSDC-A* **2014**, *34*, 3219–3239.
18. Kozlov, V.; Kuznetsov, N.; Lokharu, E. Solitary waves on constant vorticity flows with an interior stagnation point. *J. Fluid. Mech.* **2020**, *904*, A4. [CrossRef]
19. Dyachenko, A.; Zakharov, V.; Kuznetsov, E. Nonlinear dynamics of the free surface of an ideal fluid. *Plasma Phys.* **1996**, *22*, 916–928.
20. Choi, W. Strongly nonlinear long gravity waves in uniform shear flows. *Phys. Rev. E* **2003**, *68*, 026305. [CrossRef]
21. Milewski, P.; Vanden-Broeck, J.; Wang, Z. Dynamics of steep two-dimensional gravity-capillary solitary waves. *J. Fluid Mech.* **2010**, *664*, 466–477. [CrossRef]
22. Flamarion, M.V.; Ribeiro, R., Jr. An iterative method to compute conformal mappings and their inverses in the context of water waves over topographies. *Int. J. Numer. Methods Fluids* **2021**, *93*, 3304–3311. [CrossRef]
23. Trefethen, L.N. *Spectral Methods in MATLAB*; SIAM: Philadelphia, PA, USA, 2001.
24. Ko, J.; Strauss, W. Large-amplitude steady rotational water waves. *Eur. J. Mech.* **2008**, *27*, 96–109. [CrossRef]
25. Guan X. Particle trajectories under interactions between solitary waves and a linear shear current. *Theor. Appl. Mech. Lett.* **2020**, *10*, 125–131. [CrossRef]